Nanoscale

PAPER

View Article Online
View Journal

Cite this: DOI: 10.1039/d5nr04782j

Process-dependent hypersonic phonon dispersion of brush particle metamaterials

Qiqi Li,[a,d] Iyad Ramdane,[b] Jirameth Tarnsangpradit,[c] Pascal Rembert,[b] Rebecca Sainidou,[b] Yu Cang,[d] Krzysztof Matyjaszewski,[e,f] Michael R. Bockstaller,[c] Bartłomiej Graczykowski[g] and George Fytas *[a,g,h]

The self-assembly of polymer-grafted nanoparticles (PGN) has drawn interest as a platform approach for the fabrication of hybrid materials in which novel functionalities, such as photonic or phononic band gap formation, arise from the interplay of microstructure regularity and brush interactions. However, the complex dynamical processes associated with polymer and particle constituents render PGN assembly structures susceptible for the arrest of metastable states and impart sensitivity of physical properties to process conditions. For the case of poly(methyl methacrylate) (PMMA)-grafted silica particles, the use of volatile solvents (such as tetrahydrofuran) during film formation results in metastable microstructures with reduced effective medium sound velocity but increased width of the band gap as compared to equilibrated films cast from toluene solution. The linear acoustic dispersion obtained from Brillouin light spectroscopy combined with elastodynamic calculations suggest that the use of volatile solvents increases the free volume of PMMA, while maintaining the local order of particles within the film. Surprisingly, stop-band formation was more pronounced in metastable microstructures. The origin for this unusual behavior resides in the hybridization mechanism underlying the gap formation. Thus, the increased contrast of elastic constants 'overcompensates' the loss of long-range positional order and amplifies the hybridization gap that originates from the dipolar (ℓ = 1) resonance of the SiO_2 cores coupled to the polymer grafts of neighboring PGNs.

Received 12th November 2025,
Accepted 15th February 2026

DOI: 10.1039/d5nr04782j

rsc.li/nanoscale

Introduction

Colloidal self-assembly has emerged as a facile method to realize materials for the controlled propagation of light.[1–11] The long-range order of these materials, known as 'artificial opals', is responsible for the appearance of structural colors (*via* a mechanism akin to Bragg diffraction). Since physical properties of crystal structures are directional, such interference-induced structural colors depend on parameters like the angles of incidence and observation. Under certain conditions, such as suitable optical characteristics of constituents, structural color can be preserved in the disordered state. Such photonic glasses feature isotropic structural color that arises from Mie resonances of particles and short-range positional correlations manifested in the structure factor of the colloidal assembly.[7,8] Colloidal photonic crystals and glasses can also control the flow of sound over a broad frequency range.[12–15] In particular, hypersonic (GHz) phonons commensurate with photons in the visible spectrum and structures with submicron spacing can host strong photon-phonon interactions.[16–18] While Bragg diffraction is the primary mechanism of the stop band formation in both photonic and phononic crystals, the formation of a second, so called hybridization phononic stop band (HG) at lower frequencies, that has been reported for both colloidal crystals and glasses,[19–23] has no straightforward analogy to colloidal photonics. The additional HG stopband emerges due to hybridization of propagating waves with a local resonance.[19,24] A common feature with colloidal photonics is the association of the Mie resonance and vibration eigenfrequencies with the photonic and hybridization phononic stop bands, respectively. The phononic HG occurs at higher fre-

[a]Max Planck Institute for Polymer Research, Ackermannweg 10, 55128 Mainz, Germany. E-mail: fytas@mpip-mainz.mpg.de
[b]Laboratoire Ondes et Milieux Complexes UMR CNRS 6294, UNIHAVRE Normandie University, 75 rue Bellot, Le Havre F-76600, France
[c]Department of Materials Science and Engineering, Carnegie Mellon University, 5000 Forbes Ave., Pittsburgh, Pennsylvania 15213, USA
[d]School of Aerospace Engineering and Applied Mechanics, Tongji University, Zhangwu Road 100, Shanghai 200092, China
[e]Department of Chemistry, Carnegie Mellon University, 4400 Fifth Ave., Pittsburgh, Pennsylvania 15213, USA
[f]Department of Molecular Physics, Faculty of Chemistry, Lodz University of Technology, Żeromskiego 116, 90-924 Łódź, Poland
[g]Faculty of Physics, Adam Mickiewicz University, Uniwersytetu Poznanskiego 2, Poznan 61-614, Poland
[h]Institute of Electronic Structure and Laser, 71110 Heraklion, Greece

quency than the quadrupolar ($\ell = 2$) mode of the single particle and full elastodynamic calculations have revealed the importance of interparticle contacts on the nature of the particle vibration resonance-induced HG.[24] The grafting of polymers on nanoparticle surfaces alters the properties of contact and thus the characteristics of HGs.[25] Local order in colloidal glasses has also been shown to impact the phononic band diagram, depending on the elastic and density contrast as well as the topology of the system (solid/liquid or solid/solid).[24] Besides regular crystalline and glassy systems, stop band formation has also been predicted for disordered hyperuniform structures (featuring the suppression of long wavelength fluctuations and the absence of long-range order)[26] and gradient morphologies (featuring, for example, a gradual transition of particle size).[9,27]

Polymer-grafted nanoparticles (PGN) have recently emerged as a new class of hybrid material[28,29] in which both assembly and interactions can be controlled *via* the degree of polymerization (N), density (σ) and dispersity ($Đ$) of tethered chains as well as the particle core radius (R_c).[30–32] The presence of a polymer canopy alleviates core-core contacts, dictates the local structure and determines the characteristic spacing in self-assembled PGN solids.[25] In PGN solids formed by solution casting of polystyrene (PS)-grafted silica (SiO_2) in the dense grafting regime ($\sigma > 0.5$ nm^{-2}), the phononic band diagram revealed a local-resonance induced HG with longitudinal polarization. It was assigned to the dipole resonance ($\ell = 1$) of the core interacting with the brush canopies of neighboring PGN's, assuming anisotropic elasticity across the polymer/core interface, through imperfect boundary conditions.[25,33] The role of brush interdigitation between adjacent PGN's, and its impact on phonon propagation, was not considered in the theoretical analysis. Variation of short-range positional correlations in the same PGN assembly *via* processing is needed for an unambiguous correlation to the opening of HG in PGN solids.

In densely grafted systems, the two-layer model (TLM) predicts interdigitation to be limited for $N < N^*$ where N^* denotes the degree of polymerization at which the stretching energy per chain assumes a maximum value.[31,32] Due to the slow kinetics of PGNs in the melt state, PGN solids are prone to defect formation and the persistence of metastable assembly structures that depend on process conditions. We have recently shown that the molecular friction impacts on interdigitation and glass formation in the dry powder state of poly(methyl methacrylate) (PMMA) grafted SiO_2 solids compared to SiO_2-PS analogues with similar molecular characteristics and glass transition.[34] The differences were related to the high molecular friction coefficient of MMA which reduced brush interdigitation and prolonged the fusion of metastable PGN cluster structures prepared by precipitation from aqueous solution.[35] Here, we harness the sensitivity of phonon propagation in the high frequency-range to local density fluctuations and PGN interactions to evaluate the effect of solvent processing on the hypersonic phonon dispersion characteristics of PGN solids. The dispersion relations recorded by angular–dependent Brillouin light scattering (BLS) reveal that both the effective medium sound velocity and the opening of propagation HG stopband in SiO_2-PMMA PGNs with $N = 553$ and $N = 1244$ are process- and solvent-dependent of the PGN glassy films. A more metastable PGN assembly structure results when films are cast from volatile solvents (THF) as compared to high boiling point solvents such as toluene, for which near-equilibrium structures were formed. The process-dependent HG stopband for the same PGN is not robust to disorder suggesting dependence on short-range positional correlations. Theoretical analysis of the dispersion relation illuminates the impact of solvent processing on the microstructure of PGN assemblies.

Experimental

Materials

Methyl methacrylate (MMA, 99%, Aldrich) was purified by passing through a column filled with basic alumina to remove the inhibitor. Tris(2-dimethylaminoethyl)amine (Me6TREN, 99%, Alfa), anisole (99%, Aldrich), tetrahydrofuran (THF, 99%, VWR), methanol (99%, VWR), *N*,*N*-dimethylformamide (DMF, 99%, VWR), copper(II) bromide ($CuBr_2$, 99%, Aldrich), tin(II) 2-ethylhexanoate ($Sn(EH)_2$, 95%, Aldrich), 48% hydrofluoric acid aqueous solution (HF, >99.99%, Aldrich), ammonium hydroxide aqueous solution (NH_4OH, 28.0–30.0%, Fisher). The tethered ATRP initiator 1-(chlorodimethylsilyl)propyl-2-bromoisobutyrate and surface modified silica (SiO_2-Br) were prepared using previously reported procedures.[36,37]

Synthesis of SiO_2-PMMA particle brushes *via* ARGET ATRP

The synthetic procedure followed previously published reports.[38] In short, initiator-modified SiO_2 nanoparticles stock solution, monomer (MMA), solvents (anisole), $CuBr_2$, and Me_6TREN were mixed thoroughly in a sealed Schlenk flask. Meanwhile, a stock solution of $Sn(EH)_2$ in anisole was prepared. Both mixtures were degassed by nitrogen purging, then the $Sn(EH)_2$ solution was injected into the Schlenk flask to activate the catalyst complex and the flask was immediately placed into an oil bath set at 60 °C. The conversion and molecular weight (MW) of the polymer were monitored by gravimetric analysis and size exclusion chromatography (SEC), respectively.

Film preparation

All films were prepared *via* solvent casting at room temperature on a 2 × 2 cm^2 substrate of borosilicate glass. The substrate was cleaned with isopropanol and was air-dried prior to the film preparation. Particle brush in toluene solutions were used to prepare the films. The film thickness was approximately 15 μm. To obtain the powder samples, drops of PGN solution (~0.1 mL of 10 mg mL^{-1}) were added to the methanol vial (~20 mL) and were quickly agitated using vortex mixer. The precipitates were gathered and vacuum dried in the oven for 24 h without thermal annealing.

Brillouin light spectroscopy (BLS)

BLS is a powerful, non-contact, non-destructive all-optical technique that probes phonon propagation at GHz frequencies. Utilizing the photoelastic interactions between incident light and thermally activated phonons, BLS records the spectra of inelastically scattered light by phonons with wave vector q, which (for spatially homogenous phononic crystals, there is a reciprocal lattice vector $\mathbf{q} \pm \mathbf{G}$)[39] equals to the scattering wave vector $\mathbf{k} = \pm\mathbf{q} = \mathbf{k_s} - \mathbf{k_i}$ with $\mathbf{k_s}$ and $\mathbf{k_i}$ being wave vectors of the scattered and incident light, respectively. In the transmission geometry employed in this work, the magnitude of $q = 4\pi/\lambda \sin\alpha$ is tuned by the incident angle and is independent from the refractive index n as $\alpha(= \theta/2)$ is half of the scattering angle θ. For the wavelength of the incident light λ = 532 nm q varies in the range (0.007–0.024) nm^{-1}. Higher q's in the range (0.027–0.035) nm^{-1} are accessible in the reflection geometry, where the knowledge of the medium's refractive index is required as $q = (4\pi\sqrt{n^2 - \sin^2\alpha})/\lambda$ depends on both α and n.[38] The phonon-matter coupling is manifested in the dispersion relation, $f(q)$, where the phonon frequency f is in the hypersonic (GHz)range and is resolved by a high-resolution tandem Fabry–Perot interferometer (JRS Instruments). In the simple case of homogeneously disordered materials, $f(q)$ is linear in the long-wavelength regime (wavelengths much longer than the interparticle distances) with the slope yielding the longitudinal or transverse effective medium sound velocities (depending on polarization).[40] In this work, we used two PGN samples with N = 553 and N = 1244 with spacing in the submicron range to commensurate q of BLS necessary to record the phonon band diagram.[34]

Theoretical methods

For the calculation of the dispersion curves $f(q)$ of the elastic eigenmodes of the PGN assemblies of silica particles embedded in a solid host (here PMMA), we employed a first-principles full elastodynamic formalism.[41,42] The formalism is based on a multipole expansion of the elastic field and takes into account all interactions between particles, assuming them to be non-overlapping (*i.e.*, almost touching), for close-packed structures. In this study, ordinary (perfect) boundary conditions (PBCs) are adopted across the particle-matrix interface. Band structure calculations were performed along the [111] (ΓL) direction of a face-centered cubic (fcc) crystal, assuming a spherical scatterer per unit cell, defined by three primitive lattice vectors, $\boldsymbol{a}_1 = d(1,0,0)$, $\boldsymbol{a}_2 = \frac{d}{2}(1,\sqrt{3},0)$, and $\boldsymbol{a}_3 = \frac{d}{6}(3,\sqrt{3},2\sqrt{6})$, where d is the first neighbour distance. The fcc packing has been found to be a relevant packing structure for PGN assemblies similar to those presented in this paper. We also note that the choice of crystallographic direction is not expected to appreciably affect our conclusions since calculations along the ΓL direction yield similar results to, for example, the ΓM direction that describes better the experimental situation.[12,33] Density-of-states (DOS) calculations[43] are also performed for individual particles embedded in a host matrix, to obtain the additional virtual bound states induced in these systems with respect to those of the homogeneous, infinitely extended host matrix. In this work, we model the PGN films by considering the grafted polymer as a homogeneous host medium in which silica cores are embedded by applying perfect boundary conditions across the silica-polymer interface to describe the grafting. The above scheme has been successfully used to reproduce effectively the experimental phonon dispersion.[25,33] In these systems the boundary conditions can be either perfect or imperfect (assuming discontinuity for the displacement to take into account an interphase between the two materials), but for long chains perfect boundary conditions are sufficient to describe these grafting-particle crystals. Variation of the elastic parameters of the polymer with the distance to the core has been assumed in the case of THF-casted films (see discussion in Fig. 4c below) by introducing a homogeneous PMMA shell coating the core, embedded in a softer PMMA host matrix.

Results and discussion

Quasi-equilibrium and metastable states

In the following, PGN films cast from toluene will be identified with the prefix 'PT' while THF-cast films will be identified with 'P', respectively. Two exemplary BLS spectra of PT-553 transparent film, recorded far from ($qd_{[111]}/\pi < 1$) and near ($qd_{[111]}/\pi \approx 1$) the Brillouin zone (BZ) edge assuming a fcc with ⟨111⟩ out-of-plane orientation, are shown in the upper panel of Fig. 1a. The dispersion plot $f(q)$ (deduced from the ensemble of such spectra) is depicted in Fig. 1b (filled symbols). At first glance, the two spectra display very similar patterns to those obtained for toluene-cast SiO_2-PS PGNs reported before,[33] *i.e.*, a single longitudinal acoustic peak far from the BZ edge (q = 0.0167 nm^{-1}) and a double peak near the BZ edge (q = 0.0204 nm^{-1}) occurring in the bandgap region. The latter manifests itself as a q-independent BLS intensity dip (indicative of a reduced DOS) at about 10.3 GHz (Fig. 1a, q = 0.0204 nm^{-1}) and corresponds to the middle of the gap in Fig. 1b. However, the characteristic flat band near the lower frequency limit of the gap, which was observed in toluene-cast SiO_2-PS[25,33] is not discernible in the PMMA analogues PT-553 (Fig. 1a) and PT-1244 (Fig. 3a). Rather, the contribution of this localized mode, mainly to the depolarized light scattering, was faint for SiO_2-PMMA PGNs due to their weak anisotropic scattering.

In contrast to the rather transparent appearance of the toluene-cast films, films cast from THF were opaque (*e.g.*, P-553, inset to Fig. 1b) indicating strong elastic light scattering due to a more heterogeneous microstructure that features an increased defect density (which could be formed, for example, by void or defect formation due to the rapid evaporation of solvent during the film casting process). Electron microscopy images of PGN monolayers support the formation of more metastable film structures when cast from THF solution. For example, the consistently larger apparent size of PGNs in THF-

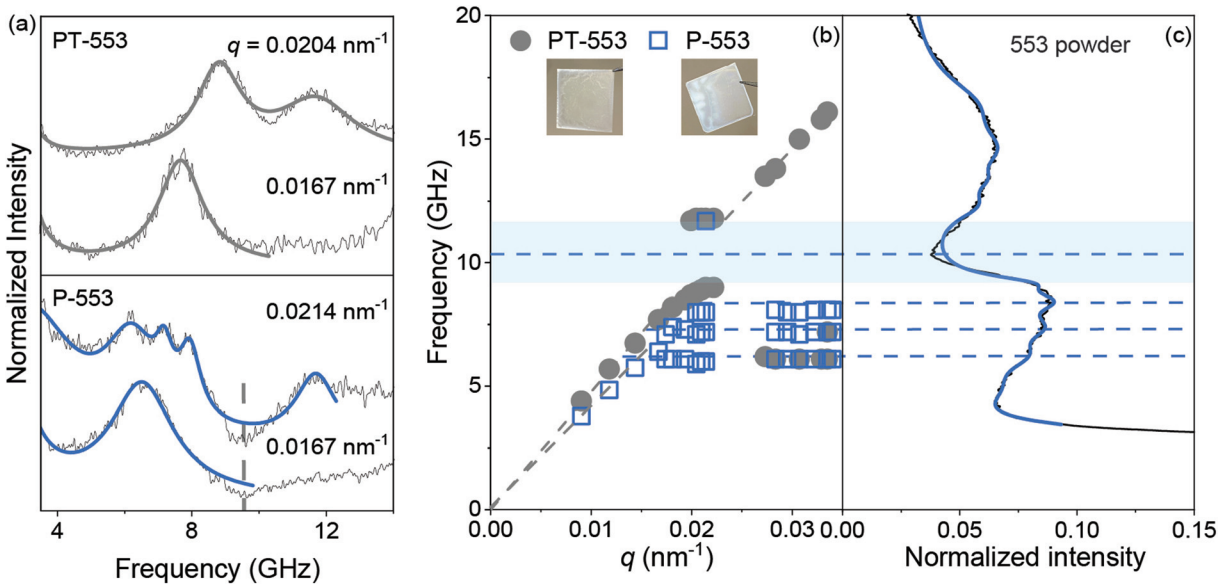

Fig. 1 (a) Polarized BLS spectra far from and near the Brillouin zone edge for films cast from THF-(P-553) and toluene-(PT-553) solution with φ_{SiO_2} = 0.31. The vertical line in the low panel and the spectrum at 0.0214 nm^{-1} indicates the frequency at the minimum (density of states) intensity. The numbers next to the spectra indicate the values of q. (b) The hypersonic phonon dispersion for the films in (a) as indicated in the legend. Insets: optical images of the films. (c) The vibration spectrum of SiO_2-PMMA-553 powder (in air). Dashed line indicates the relation of the dip in the vibration spectrum to mid-gap frequency (≈ 10 GHz) in the dispersion diagram of toluene casted PT-553 (grey solid points). The flat modes in the dispersion of P-553 solid film (blue open squares) compare well (three dashed lines) with the eigenfrequencies of the vibration spectrum of the SiO_2-PMMA-553 particles in air. Note the two flat modes in PT-553 film at q > 0.02 nm^{-1} (solid symbols).

Table 1 Molecular characteristics of PMMA grafted SiO_2 PGNs

Sample ID	σ/nm^2	N	d/nm (TEM)	d/nm (TLM)	h/nm (TEM)	h/nm (TLM)	h_{dry}/nm (TLM)	h_{inter}/nm (TLM)
P-553	0.551	553	187 ± 14	176	34 ± 10	28	25	6
P-1244	0.495	1244	280 ± 27	210	80 ± 18	45	40	10
PT-553	0.551	553	178 ± 10	176	28 ± 10	28	25	6
PT-1244	0.495	1244	234 ± 28	210	55 ± 17	45	40	10

The thickness h_{dry} of the dry (stretched) PGN region in which interdigitation is restricted, the interpenetration layer thickness, h_{inter}, and the PGN radius, R_{tot}, can be estimated from the two-layer model (TLM)[31,32] using monomer length, l_m = 0.26 nm, Kuhn length, l_K = 1.7 nm, N_K = monomers/Kuhn segment = 6.5, ρ_K = 1.1 Kuhn segments per nm^3 and core size, R_c = 59 nm. $R_{tot}^3 = R_c^3 + 3R_c^2\sigma N_K/\rho_K$, R_{tot} = 87 nm for P-553 and R_{tot} = 105 nm for P-1244. $\varphi_{SiO_2} = [1 + 3\sigma N M_{mon}/(R_c\rho N_A)]$ yields 0.31 and 0.18 for P-553 and P-1244, respectively. Note that these values are approximated by $\varphi^*_{SiO_2} = [R_{SiO_2}/(d/2)]^3 = 0.31$ for PT-553 (d = 178 nm) and $\varphi^*_{SiO_2} = 0.14$ for PT-1244 (d = 234 nm), whereas thermogravimetry led to higher volume fraction values, 0.46 for N = 553 and 0.30 for N = 1244.[34]

cast films as compared to the toluene analogues (Table 1), for which the average size is close to the TLM prediction, is indicative of frozen-in stresses and consistent with more metastable states. We note that the TLM values are mentioned as an estimation of the deviation from the thermal equilibrium. However, the scattering wave vector **q** in both systems is well defined and the BLS spectra for P-553 at two q's, far from and near the Brillouin zone are shown in the lower panel of Fig. 1a. The BLS spectra and the dispersion relation of P-553 in Fig. 1b (open symbols, left panel) are distinctly different from that in PT-553, both at low q's and at bandgap region. Comparison of the spectra for the two films reveals a red shift in the case of P-553, *i.e.*, a slow-down of the effective medium longitudinal phonon (corresponding to the single acoustic peak), at q = 0.0167 nm^{-1} with phonon wavelength $\Lambda = 2\pi/q \simeq$ 376 nm. Near the BZ edge ($q \simeq 0.0214$ nm^{-1}), the BLS intensity dip at about 9.5 GHz (Fig. 1a, lower panel) is also red-shifted. More importantly, with increasing q, the single peak evolves into a triple, composite peak, below the gap region, suggesting the presence of three modes. The high-frequency peak at about 11.3 GHz (upper branch in the gap region) is less pronounced than in the case of PT-553, likely due to the stronger contribution of backscattering for P-553.

The dispersion plot for both N = 553 films in Fig. 1b featured a material softening concerning the first acoustic phonon branch, yielding to lower sound velocity in P-553 compared to PT-553. At low q's, the effective medium sound velocity, c_{eff}, is slower (= 2590 ± 60 m s^{-1}) in the opaque P-553 film (d = 187 nm) than in the transparent PT-553 film (c_{eff} = 3000 ± 60 m s^{-1}, d = 178 nm), suggesting a reduced packing

density and/or phonon scattering from PGN "clusters".[44] The latter, however, would lead to a different dispersion relation.[45] Assuming Wood's rule of mixtures with $\varphi_{SiO_2} = 0.31$ and the elastic parameters of bulk PMMA (ρ = 1190 kg m^{-3}, c_{PMMA} = 2900 m s^{-1})[46] and silica (ρ = 2000 kg m^{-3}, c_{SiO_2} = 5480 m s^{-1}) —as determined from DOS calculations of the powder vibration spectra— the computed c = 3080 m s^{-1} captures within less than 5% the value of c_{eff} in PT-553, however, is about 20% higher than the value of c_{eff} in P-553. Consistent with the opaqueness of the P-553 film (inset to Fig. 1b), its low c_{eff} suggests a more porous structure, potentially caused by rapid solvent evaporation that reduced equilibration of the PGN microstructure.

At high q's, the position of the band gap at about 10.3 GHz for PT-553 (shaded area in Fig. 1b), decreases to ~9.5 GHz for P-553, consistent with its larger interparticle distance (d values in Table 1) and lower c_{eff}. Also, the frequency at the intensity dip scales as $\sim c_{eff}/d$ suggesting the impact of the short-range positional correlations. We note that due to the short phonon mean free-path (of the order of 1–2 μm), the local structure of near PGN neighbors is probed. In addition, the phonon dispersion for P-553 displays three localized (q-independent) modes (open squares in Fig. 1b, see also the BLS spectrum in Fig. 1a) near the edge of the BZ. Notably, these localized modes are also present in the vibration spectra of the P-553 powder (Fig. 1c). The localized modes should not be related to the eigenmodes of the individual PGN's, since the lowest (BLS active) PGN eigenmode corresponding to the quadrupolar (ℓ = 2) is predicted at about 12.5 GHz (see Fig. 2).[34] Instead, these modes (three in P553 and one in PT553, Fig. 1b) are assigned to collective vibrations of nanoparticle clusters.[34,47] Moreover, the low-DOS intensity dip in this vibration spectrum, occurring at ~10.3 GHz, coincides with the midgap frequency in PT-553 (Fig. 1b). The presence of the gap also in the PGN powder prepared by solution precipitation, implies clustering of PGNs with a local order similar to that of the P-553 films. Further, the presence of a HG corroborates the notion that the crystalline structure is not necessary for hypersonic colloid-based phononics[25] like in close-packed hard sphere colloids.[19] However, like in photonic glasses,[7,8] disorder reflected in the structure factor of the metastable states matters. In this context, PGN solids can be a platform for fabrication of disordered hyperuniform structures.[26,48,49]

Given the similar thermomechanical properties of PMMA and PS grafts, we concluded that it is the structural differences between the films prepared from toluene and THF which determine the superposition of their respective $f(q)$ (Fig. S2). We recall that in the reduced dispersion plot (fd/c_{eff} *vs.* qd), the acoustic branch, representative of the effective medium, should coincide for the different systems, whereas the first Bragg gap (assuming a fcc packing structure) should occur at $fd_{[111]}/c_{eff} = 0.5$ and $qd_{[111]}/\pi = 1$, where $d_{[111]} = d\sqrt{6}/3 \approx 0.816d$ is the spacing between consecutive (111) particle planes. Using d = 187 nm for the P-553 and d = 176 nm (almost the TLM value, Table 1) for PT-553, the reduced representations of fd/c_{eff} *vs.* qd yield a good superposition only for the acoustic branch, and the gap in PT-553 appears at $fd/c_{eff} \simeq 0.65$ and $qd \simeq 3.8$. Instead, for the superposition of the flat modes, the TLM PGN diameter value d (= 176 nm) for both films needs to be assumed (Fig. S2c). We note that the superposition of the acoustic branch (long wavelength regime of $f(q)$) appears to be insensitive to the particular choice of PGN diameter (Fig. S2), since only the experimental c_{eff} matters. We hypothesize that the sensitivity to the choice of particle size needed to obtain superposition of the short wavelength regime of $f(q)$ reflects the impact of the distinct levels of metastability in P-553 and PT-553 (the latter representing a more 'equilibrium-type' structure). The different short-range positional arrangement (local structure) between the two systems of identical PGN is reflected in the HG bandwidth (Fig. 1b and Fig. S2c). For the

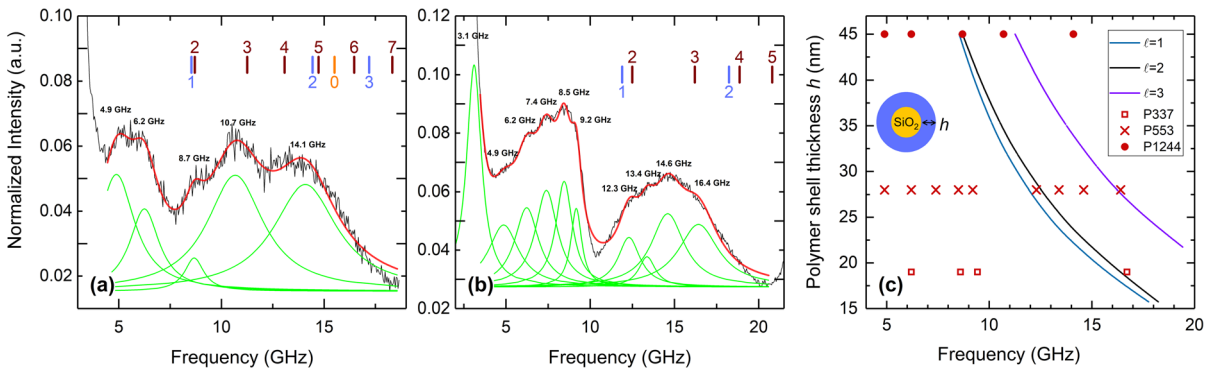

Fig. 2 The experimental vibrational spectra (black curves) of (a) P-1244 (brush particle diameter d = 210 nm) and (b) P-553 (brush particle diameter d = 176 nm) powders, fitted (red line) as a sum of Lorentzian contributions (green curves). A possible contribution of backscattering should be expected at ~14.4 GHz. The resolved Lorentzian peaks are compared to the individual spherical particle eigenmodes (vertical lines) obtained by DOS calculations assuming perfect boundary conditions (PBC) for silica cores (R_c = 59 nm) coated by PMMA shell (P-1244: h = 28 nm and P-553: h = 45 nm, Table 1). The ℓ-numbered vertical lines are color-indexed to denote different eigenmode families (see text). (c) Variation of the eigenmode frequencies of the individual brush particles (see inset) with the thickness h of the grafted PMMA obtained by DOS calculations under PBC along with the experimental data (symbols).

localized modes, the need for the use of the same TLM value for particle size suggests that the individual PGN assumes similar a structure irrespectively of the film fabrication process. Overall, the metastability in PGN films seems to result from non-equilibrium graft configurations between neighbouring PGNs which impacts the phonon dispersion of the assembled PGN films.

Particle vibrations in PGN powder

The contacts between PGNs through the grafted chains can modify the vibration spectrum of individual PGNs.[34] The eigenmode spectra of PGN powder, depicted in Fig. 2a and b, show rather unexpected features, which are absent in the vibration spectra of their equivalent SiO_2-PS (N = 600 and 1300)[50,51] counterparts. First, they exhibit an intensity dip at ~7.5 GHz and 10.3 GHz for P-1244 and P-553 that relates to the low DOS, which is the fingerprint of the band gap, *e.g.*, Fig. 1b for P-553. Second, we observe resolved modes with frequencies below the dip. The eigenmodes of independent PGNs (Fig. 2c) are expected at frequencies above the gap frequency, near the upper frequency branch of the band (Fig. 1b),[25,33] as confirmed by theoretical DOS calculations.[43] The frequency positions of the calculated spheroidal eigenmodes of an individual spherical particle (diameter $d_c = 2R_c$ = 120 nm) coated by a homogeneous PMMA shell of thickness h, immersed in air, are indicated by small vertical lines at the top in Fig. 2a and b.

The eigenmodes are characterized by the angular momentum number ℓ assigned to each line. The calculations assume perfect boundary conditions (PBC) across the silica-PMMA interface, and the position of each mode is extracted from the Lorentzian peaks representing the density of states (DOS) of the elastic field of a single scatterer. The spheroidal eigenmodes belong to three subfamilies[50] which are distinguished by different colors in the spectra of Fig. 2a and b. The shell-localized, mostly radial vibrations (red lines), are usually well discernible in the BLS spectra of PGN powders. In contrast, the mostly tangential vibrations localized in both shell and core (blue lines) are not discernible in the BLS spectra. The isotropic monopolar (ℓ = 0), breathing vibration is also present (orange line). For both P-1244 and P-553 powder spectra, the DOS-calculated eigenmodes of the individual spherical SiO_2-PMMA particles in air occur just above the frequency of the dip, at 7.5 GHz and 10.3 GHz, respectively. They coincide with the broad frequency peaks in these spectra (*e.g.*, centered at f ≈ 15 GHz in Fig. 2b), for which, however, a fine structure (ℓ = 2, 3, ...) can clearly be discerned in the spectra. Therefore, these individual particle eigenmodes cannot be assigned to the experimentally resolved peaks of the powder spectra occurring below these dips. The difference between PMMA-PGNs as compared to the earlier SiO_2-PS PGNs[50,51] is indeed surprising given their similar structure and glass transition temperature, T_g, and indicative of a more profound impact of brush composition on PGN interactions in the film state.

Alternatively, the low-frequency modes in $I(f)$ vibration spectrum and a broad peak at ~8.7 GHz in the power $f^2I(f)$ spectrum of P553 (Fig. S3) should result from interactions between individual PGNs and fall below the mid-gap frequency in Fig. 1b. The assignment of the low frequency modes to PGN clusters is also supported by the position of the calculated eigenfrequencies of the individual particles (Fig. 2a and b). The appearance of the low frequency flat modes in the dispersion of P-553 film (Fig. 1b) implies PGN clustering, similar to the powder. We note that the vibration spectrum of the powder corresponds to a backscattering q, due to the opaque sample.[27] The evolution of the frequency-resolved peaks of the vibration spectra with the variation of the shell thickness h is depicted in Fig. 2c for the three particle powders, P-1244, P-553 and P-337 (the latter is characterized by N = 337, σ = 0.557 nm^{-2}, d = 158 ± 7 nm and h = 19 nm), together with the DOS-calculated spheroidal eigenfrequencies for the first three lowest frequency modes (ℓ = 1,2, and 3). For all three systems, the experimentally resolved peaks are organized into two subgroups, separated by a region without modes in it (the so-called dip), whose center follows the general shape of the theoretical dispersion lines $h(f)$, and more surprisingly the upper frequency limit of this region coincides with the first spheroidal calculated line.

Given the metastability of the present PGN films, we record the dispersion relation and the vibration spectra of the powder after heating the different solvent-cast films at 410 K, above T_g = 383 K of PMMA. As seen in Fig. S3, the vibration spectrum is robust to the thermal annealing implying reversible GPN interactions due to trapped configuration as opposed to SiO_2-PS PNG with similar N and σ, for which the spectrum reflects a bulk PS structure through melting and entanglement of the PS grafts after heating above T_g.[34] Given the similar T_g of PS and PMMA, and the similar graft characteristics, we conclude that the differences are due to much slower dynamics of PMMA as inferred from both lower entanglement molecular weight for PMMA (13.6 kDa) compared to PS (18.1 kDa)[52] and the significantly larger molecular friction between MMA repeats.[53] Moreover, the two polymers display different non-Arrhenius temperature dependence of the monomer friction coefficient.[34,53] In a similar context, polymer brush configuration leads to a reduced thermal expansion as compared to spin-cast film of the same polymer of similar thickness that renders the evidence of T_g in the former weaker.[34,54] The significantly lower mobility in PMMA renders thermal annealing less effective to equilibrate the film microstructure.[33] Thus, the phonon dispersion relation of the annealed P-553 film remains unchanged apart of the increase of c_{eff} (= 2700 m s^{-1}) which can be attributed to an increased packing density compared to the as-cast counterpart. However, the increase of c_{eff} (~5%) is still well below the expected value (c_{eff} = 3080 m s^{-1}) which is measured in PT-553 suggesting a less distinctive structural change upon annealing.

Process-dependent hypersonic phonon dispersion

The BLS spectra of P-1244 (opaque film) at two q values close to the BZ edge are shown in the lower panel of Fig. 3a, revealing a q-insensitive double peak which is reminiscent of proxi-

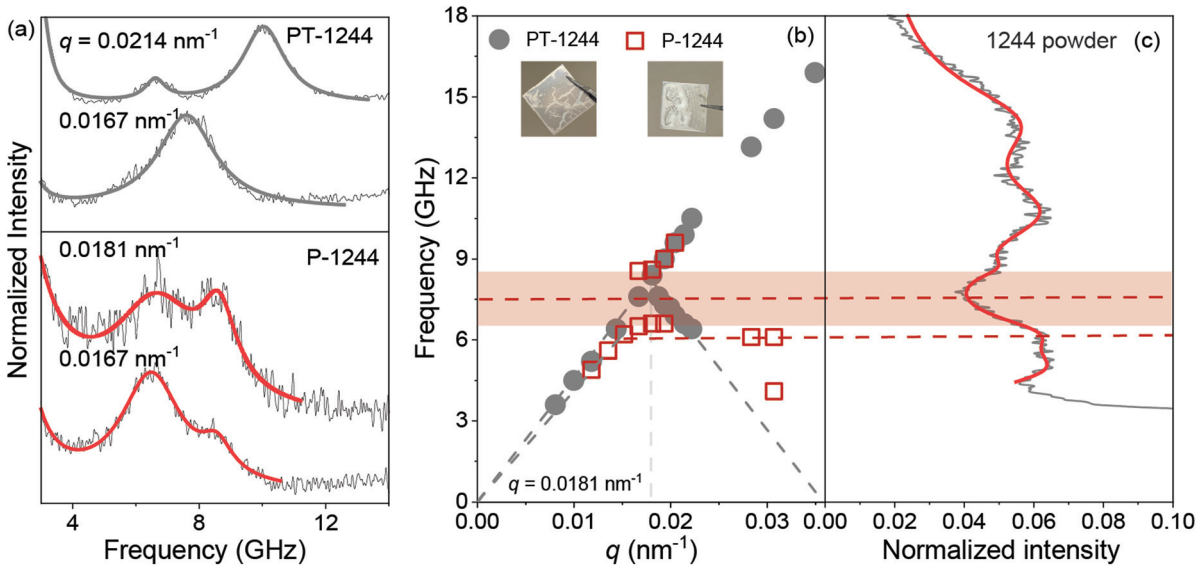

Fig. 3 (a) Polarized spectra far below and near the BZ edge for THF-cased (P-1244) and toluene-casted (PT-1244) SiO_2-PMMA-1244 with φ_{SiO_2} = 0.18. (b) The hypersonic phonon dispersion for the films in (a). Insets: optical images. (c) The vibration spectrum of SiO_2-PMMA-1244 powder (in air). Dashed line indicates the relation of the dip in the vibration spectrum to the midgap frequency (at 7.5 GHz) in the dispersion diagram of PT-1244 (grey solid points). The flat modes in the dispersion of P-1244 (open red squares) compare well (one dashed line) with the eigenfrequencies of the vibration spectrum in (c).

mity to a bandgap with flattening of the dispersion curve. Accordingly, the dispersion plot (Fig. 3b, open symbols) reveals c_{eff} = 2530 ± 50 m s^{-1} and a bandgap opening at ~7.5 GHz. Both frequency position and width coincide with those of the dip of the powder vibration spectrum (Fig. 3c). The gap appears at lower q-values than in the case of P-553 (Fig. 1b) due to the larger (≃ 60%) spacing for the P-1244 film (d = 280 nm, Table 1). In comparison, the main peak of the BLS spectrum of PT-1244 (transparent) at a similar q, shown in the upper part of Fig. 3a, is attributed to the acoustic branch, as it increases linearly with q. In contrast, the dispersion of PT-1244 in Fig. 3b (filled symbols) displays a single longitudinal acoustic phonon with no discernible bandgap; the absence of bandgap is not direction-dependent as verified through rotation of the film. This is an unexpected observation in view of the ordered PT-1244 film, that is evident from the presence of the Bragg branch $\omega = c(-q + 2\pi/d_{[111]})$[55] with c = 2900 ± 60 m s^{-1} and d = 234 nm; note that the slope of the linear acoustic branch (solid points) in Fig. 3b yields c_{eff} = 2960 ± 60 m s^{-1}. A probable explanation of the absence of bandgap is the low φ_{SiO_2} (0.18) in the PT-1244 film and the lower elastic impedance mismatch between pristine PMMA (E = 6 GPa *vs.* 4 GPa for PS)[46] and SiO_2 compared to the corresponding SiO_2-PS PGNs.[25,33] However, this assertion does not apparently apply to the THF-cast analogue, P-1244, which displays a bandgap at ~7.5 GHz (Fig. 3b). Hence, we attribute the distinct dispersion characteristics between P-1244 and PT-1244 to fabrication-induced differences in their local structure.

Observation of the two acoustic branches (open and filled symbols) in Fig. 3b reveals that c_{eff} in the opaque P-1244 film is about 15% lower than that of the transparent PT-1244 film. The latter is well captured by Wood's rule of mixtures with φ_{SiO_2} = 0.18 yielding c = 2960 ± 50 m s^{-1}, which exceeds (by 17%) the experimental value in P-1244 (THF casted) film. Consistent with the opaqueness of this film (inset in Fig. 3b), its low c_{eff} suggests a more porous structure (as compared to P-553, Section Quasi-equilibrium and metastable states), possibly caused by the higher vapor pressure of THF that could promote void formation during solvent evaporation. Notably, c_{eff} of the metastable P-553 and P-1244 films deviated by the same amount (~20%) from the quasi-equilibrium PGN films for both N values. Here, it is noted that TEM analysis of PGN monolayers (see Fig. S1) revealed a larger average diameter of PGNs in films cast from THF (d = 280 nm) as compared to toluene (d = 234 nm).

The formation of a large HG in the THF-cast P-1244 film compared to the very narrow (almost closed) band gap in the more uniform PT-1244 is notable and underscores the role of interactions that overcome the periodic order for the formation of HGs. Recall that the HG in SiO_2-PS PGNs was assigned to the dipole (ℓ = 1) mode of the SiO_2-core and its coupling to neighboring cores.[33] Hence, HG formation is expected to be influenced by the local structure as well as the impedance mismatch due to the presence of voids between core and brush components. As in the case of P-553 (Section Quasi-equilibrium and metastable states), we conclude that, in systems featuring suitable short-range positional correlations the formation of defects (such as voids or nanoporosity) can actually promote band gap formation, for example, by amplification of the impedance mismatch (as evidenced by the reduced c_{eff}). This surprising observation counters the established view of structural regularity being a prerequisite of band gap for-

mation and provides new opportunities for the use of self-assembly for the fabrication of phononic band gap materials. We recall that, assuming equal packing structure, in the normalized representation fd/c_{eff} *vs.* qd, a Bragg gap should occur at the same position (*i.e.*, $fd/c_{\mathrm{eff}} \simeq 0.65$ and $qd \simeq 3.8$, Fig. S3) irrespective of the sample composition. Variation of d using a trial-and-error approach to better match experimental results for P-1244 did not yield satisfactory results (Fig. S4). Using as a benchmark the reduced band diagram of PT-1244 (d = 234 nm), which displayed a very narrow gap at almost the same loci ($fd/c_{\mathrm{eff}} \simeq 0.65$ and $qd \simeq 4$) as the PT-553 counterpart ($fd/c_{\mathrm{eff}} \simeq 0.65$ and $qd \simeq 3.8$), none of the assumed d values (280 nm and 234 nm, Table 1) was capable of reproducing results for P-1244, as shown in Fig. S4a and b. The gap in P-1244 occurs at $fd/c_{\mathrm{eff}} \simeq 0.82$ and $qd \simeq 5.0$ for d = 280 nm, significantly higher than in PT-1244. The discrepancy in the reduced band diagram, which also manifests itself in the lack of superposition of the upper branch in both P-1244 and PT-1244 PGN solids, might imply an even smaller effective local d_{loc}. In fact, a successful superposition (Fig. S4c) is obtained using a reduced d_{loc} (~210 nm) for P-1244, close to the TLM prediction (Table 1). Unlike P-553 and PT-553 which both featured a bandgap with different width (Fig. 1b and Fig. S2c), the absence of a stop band in PT-1244 implies a different local structure than for P-1244. This conclusion was further supported by the discrepancy in the bandwidth and the midgap frequency of the HG gap (Fig. 3c) Thus, in the case of N = 1244, we find that processing impacts both local and global structure. Similar to P-553, the reduced c_{eff} is suggestive of a porous structure. As for the lower molecular analogue, the preparation of films in toluene (PT-1244) results in more equilibrated film microstructures with higher c_{eff} and a virtually closed HG.

The (powder) eigenmode spectrum of P-1244, shown in Fig. 2, exhibited the same unexpected features, as its P-553 counterpart (Fig. 2b), *i.e.*, an intensity dip at ~7.5 GHz (compared to 10.3 GHz for P-553) and resolved modes with frequencies below this dip (gap). The different frequency positions of the dip scale as $1/d$ for the two systems. The powder spectrum of P-1244 (Fig. 2a) corroborates the conclusions for the case of P-553: first, the vibration peaks below the gap frequency do not correspond to eigenfrequencies of isolated P-1244 PGN, which would be expected at frequencies above the upper gap limit (Fig. 3b). Second, the low frequency modes in $I(f)$ vibration spectrum or a broad peak at ~6.5 GHz in the power $f^2I(f)$ spectrum should result from the interactions between PGNs[47] falling below the midgap frequency in Fig. 3b.[24,29]

Since the P-1244 film is also metastable, we follow similar steps to reveal the dependence of its dispersion response to heating. We recorded the dispersion relation and the vibration spectra of the powder after heating of the solvent casted films at 410 K ($>T_g$). The vibration spectrum is robust to the thermal annealing thus confirming the reduced mobility of PMMA chains that was concluded from the low molecular P-553/PT-553 analogues. This implies reversible PGN interactions due to weak graft interpenetration since otherwise the spectrum would reflect a bulk PMMA film. The phonon dispersion relation appears unchanged after thermal annealing both in the case of P-1244 as for PT-1244, which is remarkable given the high PMMA volume fraction in both PGN systems. The smooth dispersion relation in Fig. 1b and 3b for in-plane ($q < 0.025\mathrm{nm}^{-1}$ in transmission) and out-of-plane ($q > 0.025\mathrm{nm}^{-1}$ in reflection geometry) is strong evidence of the absence of structural anisotropy.

Calculating band structures in metastable PGN Solids

For the theoretical calculation of band diagrams, PBC are assumed to avoid additional free parameters in the absence of the flat mode f_{LO} in the experimental dispersion, in contrast to SiO_2-PS PGN films.[33] In Fig. 4 we show the calculated dispersion relation $f(q)$ along the [111] direction[12,33] of a fcc packing of silica particles (R_c = 59 nm) with nearest neighbor distance d, and embedded in homogeneous PMMA host, for both PT-553 [Fig. 4a, d = 176 nm] and PT-1244 [Fig. 4b, d = 218 nm]; the utilized elastic parameters are: ρ = 2000 kg m^{-3}, c_L = 5480 m s^{-1}, c_T = 3450 m s^{-1} for SiO_2 and ρ = 1190 kg m^{-3}, c_L = 2900 m s^{-1}, c_T = 1450 m s^{-1} for PMMA, as determined from the powder BLS spectra.[34] The theoretical calculations provide a plethora of eigenmodes along the ΓL high symmetry line of the BZ which are classified into three symmetry families: longitudinal modes (Λ_1 symmetry, dark-blue solid lines) that are usually active in BLS experiments; transverse modes (Λ_3 symmetry, light-blue solid lines) which are difficult to observe in BLS spectra due to weak amplitude,[33] and deaf modes (Λ_2 symmetry, blue dotted lines), whose lowest frequency band —centered at about 9.5 GHz in (a) and 7.7 GHz in (b)— is a flat dipole rotational mode observed previously in some SiO_2-PS PGNs systems.[33] In the present case, neither transverse, nor deaf modes were detected experimentally; the absence of the latter is probably due to low anisotropic light scattering and the rich low frequency branch (Fig. 2a and b) in the present PGNs which is absent in their PS analogues. Focusing only on the longitudinal eigenmodes of these crystal films, the theoretical picture reveals an effective-medium acoustic branch (with linear dispersion at the long wavelength limit) followed by a frequency gap region (blue-shaded area), as a result of an avoided-crossing of a dipole-resonant band of individual particles with the collective effective medium band.[33] Under the assumption of a fcc crystalline structure for PT-553 and PT-1244, the origin of the HG as well as the flat band f_{LO} (dotted lines in Fig. 4a and b) are theoretically assigned to dipole core modes; the theoretical predictions capture the experimental low frequency band branch and approximate the bandwidth. The bandwidth decreases (from ~1.4 GHz to 0.5 GHz) with decreasing filling fraction of silica (PT-553: φ_{SiO_2} = 0.31; PT-1244: φ_{SiO_2} = 0.18). This is in qualitative agreement with the experimental data, for the toluene-cast films.

However, the main experimentally resolved dispersion features, c_{eff}, and the position (center $f_G = (f_{\max} + f_{\min})/2$) and width of the gap, $\Delta f = f_{\max} - f_{\min}$, are not consistently repro-

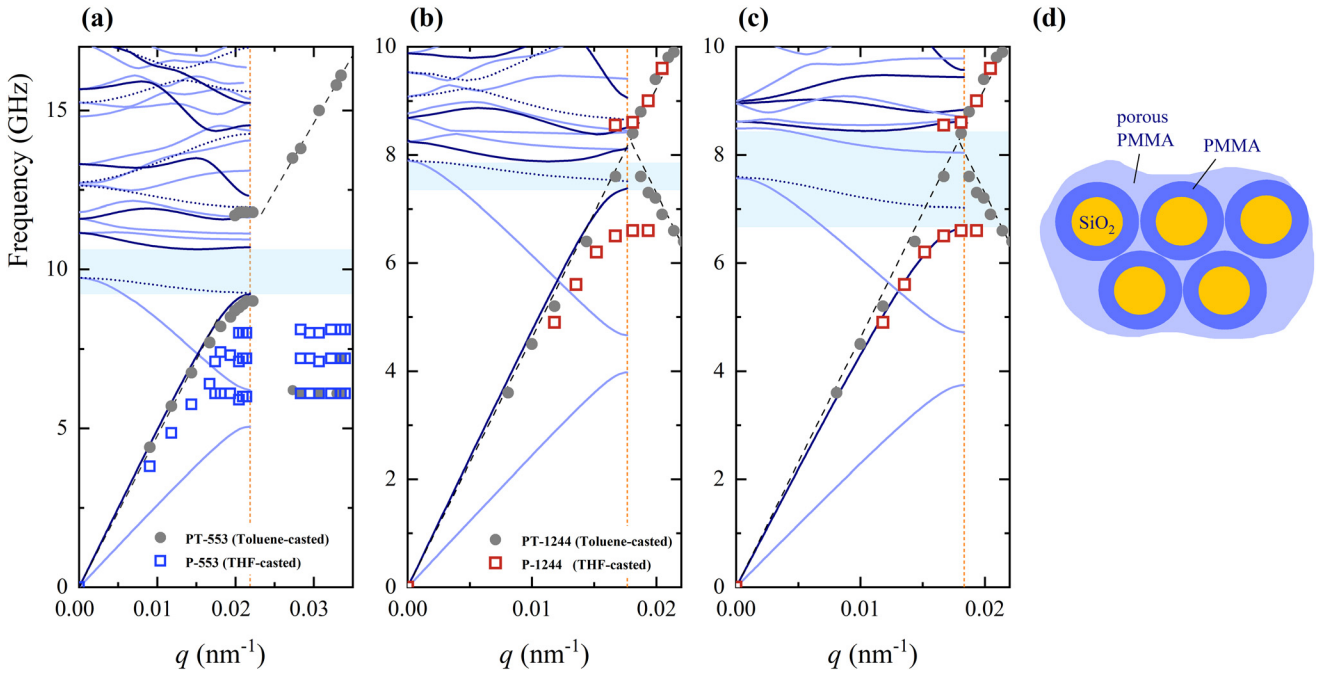

Fig. 4 Calculated band structure for (a) PT-553 (d = 176 nm TLM) and (b) PT-1244 (d = 218 nm) along [111] direction of fcc lattice (BZ limit: vertical orange dashed line) assuming PBC for silica particles embedded in PMMA host. Dark/light blue solid lines: longitudinal/transverse modes; blue-dotted lines: deaf modes. Shaded regions: frequency band gaps for longitudinal modes. (c) As in (b), but with d = 210 nm, assuming a PMMA shell depicted in (d) (shell thickness $h = h_{dry}$ = 45 nm) and a softer PMMA host matrix (mass density and longitudinal and transverse speeds are, respectively, 38%, 20% and 13% lower than those of the PMMA shell) to account for voids (porosity) in the THF casted P-1244 films.

duced for both toluene-cast films. In Fig. 4a, the theoretical dispersion replicates rather well the PT-553 experimental data. We calculate c_{eff} = 3150 m s^{-1} and $[f_{min}, f_{max}]$ = [9.2, 10.6] GHz compared to the experimental values c_{eff} = 3000 ± 60 m s^{-1} and [9.0, 11.7] GHz. In the case of PT-1244 (Fig. 4b) the calculated and experimental c_{eff} accounts to 3020 m s^{-1} and 2960 ± 60 m s^{-1}, respectively. A minor overestimation of c_{eff} and f_{min} is observed, suggesting a particle spacing close to the TLM d-value. The experimentally detected gap seems to be wider than the theoretical one, since the predicted flat, longitudinal band centered at about 11 GHz is absent in the BLS spectra. Similarly for Fig. 4b, the theoretical dispersion is found to slightly overestimate both c_{eff} and the gap width for the PT-1244 film assuming d = 218 nm. Here, we note that d = 218 nm (close to the TLM prediction) has been selected to provide a BZ edge value at $q_{BZ} = \pi/d_{[111]} = 3\pi/(\sqrt{6}d)$ = 0.0176 nm^{-1}, very close to the experimental estimate (intersection of two linear dispersion curves emerging at q = 0 and q = $2q_{BZ}$, with positive and negative slope, respectively, see dashed lines in Fig. 4b and c). The choice of d = 218 nm used in the calculations is the result of a fine tuning between the two available d-values d = 234 nm (TEM value) or d = 210 nm (TLM value) as shown in Fig. S5. We note that the conformity of the $d_{[111]}$ value to the lattice parameter for a fcc packing rather than for a bcc packing[56] is in favor of the assumed fcc lattice in the simulations. The underestimation of the theoretical bandwidth, Δf, however, indicates deviation of the real local structure from that assumed in the simulations also supported from the process-dependent experimental dispersion relations in the two PGN's (Fig. 4a and b).

We conclude that our theoretical description, assuming silica cores in a homogeneous PMMA host, successfully captures c_{eff} for both PT-553 and PT-1244. However, this modeling scheme fails to capture the experimental data for the case of THF-casted samples. Obviously, these metastable films exhibit a softer collective behaviour that manifests itself by a lowering in the experimental c_{eff} (P-553: c_{eff} = 2560 ± 30 m s^{-1}; P-1244: c_{eff} = 2530 ± 50 m s^{-1}), strongly overestimated in the theoretical calculation shown in Fig. 4a and b, corroborating the existence of trapped voids (*i.e.*, increased free volume) in the two metastable films. To account for the different levels of free volume in the simulations, we introduce a PMMA shell with elastic parameters as those for the toluene-cast films, coating the SiO_2 cores, and embed these complex particles in a softer PMMA host by assuming it to be porous (Fig. 4d). In practice, this is realized through a two-step calculation. First, a composite medium of homogeneous PMMA including void spaces with a size that is small compared to the phonon wavelength and with volume filling fraction of 38%, was assumed. The effective-medium elastic parameters of the polymer/air composite were deduced as: ρ = 738 kg m^{-3} (−38%), c_L = 2300 m s^{-1} (−20%), c_T = 1255 m s^{-1} (−13%).[57] The resulting porous PMMA is lighter and softer than the denser bulk PMMA; the relative deviation is provided in parenthesis. In a second step, the softer PMMA medium was considered as a host matrix in which SiO_2 particles were embedded and coated with the

initial homogeneous PMMA shell of thickness $h = h_{dry} =$ 45 nm; the first-neighbour distance is $d = d_c + 2h_{dry} = 210$ nm. The softer PMMA constructed in that manner simulated a porous matrix. The fraction of voids was adjusted to attain agreement between theoretical and experimental branches. The corresponding calculation shown in Fig. 4c reproduced both c_{eff}, gap-width and position of the experimental dispersion for the P-1244 film emphasizing the sensitivity of the bandgap region to the short-range order of PGNs. We note in passing that these core–shell particles are considered as non-overlapping, almost touching in the above calculations (Fig. 4d). If one considers the above particles in contact (*i.e.*, with nonzero indentation depth $0.02d$) the corresponding FEM calculations produce slightly higher c_{eff} values of the order of 2%, with respect to our multiple scattering calculations, but they do not modify the overall conclusions from the dispersion diagram.

Conclusions

Hybrid materials based on PGN assembly structures have drawn attention due to the opportunities for novel functional material design. However, the complex dynamical processes, spanning across a wide range of time- and length- scales, render PGN assembly structures susceptible for the arrest of metastable states and impart sensitivity to process conditions. This work demonstrates that the phonon dispersion in PGN assembly structures (in the hypersonic frequency regime) sensitively depends on the choice of solvent and thermal process conditions. The analysis of phonon dispersion in the long (*i.e.*, effective medium) and short (*i.e.*, near the Bragg band gap) wavelength regimes reveals information about the global and local structure of PGN assemblies. For the case of poly(methyl methacrylate) (PMMA)-grafted silica particles the results reveal that casting from THF solution results in metastable films with reduced effective medium sound velocity, but increased band gap width as compared to more equilibrated films cast from toluene solution. The low-q acoustic dispersion suggested that the use of volatile solvents during film fabrication increased the fractional free volume of PMMA while maintaining local order of particles within the film. An intriguing observation was that stop-band formation was more pronounced in metastable microstructures suggesting that the increased contrast of (effective) elastic constants 'overcompensated' any detrimental effect associated with a loss of long-range order. This confirms prior reports that suggested gap formation in PGN assembly structures not being tied to long-range periodicity (as in the case of Bragg gaps) but rather to the interaction between resonant states of adjacent particles and the resulting avoided crossing effects (*i.e.*, hybridization gap formation). Interestingly, the effect of metastable states was more pronounced for PMMA as compared to (previously studied) PS analogs under equivalent conditions. This points to salient consequences of chemical composition (due to, *e.g.*, differences in the entanglement molecular weight and local friction between repeats) that should be considered for the fabrication of film structures with deliberately controlled dispersion characteristics. Aging experiments would be beneficial to yield more information on the processing dependent states of the PNG solid films. In a similar context, an interesting aspect for future studies would also be the elucidation of the origin of defect formation in various solvent systems, to differentiate the role of solvent evaporation from external parameters such as humidity.

Author contributions

M. R. B., K. M. and G. F. designed the research; J. T., K. M., and M. R. B. synthesized particles and prepared samples; Q. L. and B. G. collected the experimental data; Q. L., B. G., Y. C., M. R. B. and G. F. analyzed data; I. R., P. R., and R. S. contributed to the theory and computer calculation; and P. R., R. S., M. R. B., and G. F. wrote the manuscript.

Conflicts of interest

There are no conflicts to declare.

Data availability

The data supporting this article have been included as part of the supplementary information.

Acknowledgements

G. F. and B. G. thank NCN (UMO-2023/51/B/ST3/01995) for financial support. The authors further acknowledge financial support by the National Science Foundation *via* DMR 2209587 (MB) and DMR 2202747 (KM). Y. C. thank the National Key R & D Project from the Ministry of Science and Technology of China (No. 2024YFA1207900) for financial support and the National Natural Science Foundation of China (Grants No. 12572160). Open Access funding provided by the Max Planck Society.

References

1 S. G. J. John, D. Joannopoulos, J. N. Winn and R. D. Meade, *Photonic crystals: Molding the flow of light*, New Jersey, United States, 2011.
2 C. T. Chan, *Phys. Rev. Lett.*, 2025, **135**, 080001.
3 Q. Zhao, C. E. Finlayson, D. R. E. Snoswell, A. Haines, C. Schäfer, P. Spahn, G. P. Hellmann, A. V. Petukhov, L. Herrmann, P. Burdet, P. A. Midgley, S. Butler, M. Mackley, Q. Guo and J. J. Baumberg, *Nat. Commun.*, 2016, 7, 11661.

4 Y. Cho, S. H. Park, M. Kwon, H. H. Kim, J.-H. Huh and S. Lee, *Adv. Mater.*, 2024, **36**, 2470174.
5 P. D. García, R. Sapienza and C. López, *Adv. Mater.*, 2010, **22**, 12–19.
6 J. D. Forster, H. Noh, S. F. Liew, V. Saranathan, C. F. Schreck, L. Yang, J.-G. Park, R. O. Prum, S. G. J. Mochrie, C. S. O'Hern, H. Cao and E. R. Dufresne, *Adv. Mater.*, 2010, **22**, 2939–2944.
7 L. Schertel, L. Siedentop, J.-M. Meijer, P. Keim, C. M. Aegerter, G. J. Aubry and G. Maret, *Adv. Opt. Mater.*, 2019, **7**, 1900442.
8 A. F. Demirörs, K. Manne, S. Magkiriadou and F. Scheffold, *Soft Matter*, 2024, **20**, 1620–1628.
9 M. Schöttle, T. Lauster, L. J. Roemling, N. Vogel and M. Retsch, *Adv. Mater.*, 2023, **35**, 2208745.
10 I. Jurewicz, A. A. K. King, R. Shanker, M. J. Large, R. J. Smith, R. Maspero, S. P. Ogilvie, J. Scheerder, J. Han, C. Backes, J. M. Razal, M. Florescu, J. L. Keddie, J. N. Coleman and A. B. Dalton, *Adv. Funct. Mater.*, 2020, **30**, 2002473.
11 C. Bittner, G. Bleyer, N. Nees, M. Carneiro, L. Pflug, M. Stingl and N. Vogel, *Adv. Mater. Interfaces*, 2024, **11**, 2300986.
12 W. Cheng, J. Wang, U. Jonas, G. Fytas and N. Stefanou, *Nat. Mater.*, 2006, **5**, 830–836.
13 M. Maldovan, *Nature*, 2013, **503**, 209–217.
14 M. Jansen, W. A. Tisdale and V. Wood, *Nat. Mater.*, 2023, **22**, 161–169.
15 T. Vasileiadis, J. Varghese, V. Babacic, J. Gomis-Bresco, D. Navarro Urrios and B. Graczykowski, *J. Appl. Phys.*, 2021, **129**, 160901.
16 J.-H. Lee, J. P. Singer and E. L. Thomas, *Adv. Mater.*, 2012, **24**, 4782–4810.
17 Y. Cang, Y. Jin, B. Djafari-Rouhani and G. Fytas, *J. Phys. D: Appl. Phys.*, 2022, **55**, 193002.
18 Y. Cang, J. Lee, Z. Wang, J. Yan, K. Matyjaszewski, M. R. Bockstaller and G. Fytas, *Adv. Mater.*, 2021, **33**, 2004732.
19 T. Still, W. Cheng, M. Retsch, R. Sainidou, J. Wang, U. Jonas, N. Stefanou and G. Fytas, *Phys. Rev. Lett.*, 2008, **100**, 194301.
20 A. V. Akimov, Y. Tanaka, A. B. Pevtsov, S. F. Kaplan, V. G. Golubev, S. Tamura, D. R. Yakovlev and M. Bayer, *Phys. Rev. Lett.*, 2008, **101**, 033902.
21 G. Zhu, N. Z. Swinteck, S. Wu, J. S. Zhang, H. Pan, J. D. Bass, P. A. Deymier, D. Banerjee and K. Yano, *Phys. Rev. B: Condens. Matter Mater. Phys.*, 2013, **88**, 144307.
22 P. J. Beltramo, D. Schneider, G. Fytas and E. M. Furst, *Phys. Rev. Lett.*, 2014, **113**, 205503.
23 H. Kim, A. Gueddida, Z. Wang, B. Djafari-Rouhani, G. Fytas and E. M. Furst, *ACS Nano*, 2023, **17**, 19224–19231.
24 Y. Cang, R. Sainidou, P. Rembert, G. Magnabosco, T. Still, N. Vogel, B. Graczykowski and G. Fytas, *J. Phys. Chem. B*, 2022, **126**, 6575–6584.
25 Y. Cang, R. Sainidou, P. Rembert, K. Matyjaszewski, M. Bockstaller, B. Graczykowski and G. Fytas, *Small*, 2024, **20**, 2304157.
26 G. Gkantzounis, T. Amoah and M. Florescu, *Phys. Rev. B*, 2017, **95**, 094120.
27 T. Vasileiadis, M. Schöttle, M. Theis, M. Retsch, G. Fytas and B. Graczykowski, *Small Methods*, 2025, **9**, 2400855.
28 J. Choi, H. Dong, K. Matyjaszewski and M. R. Bockstaller, *J. Am. Chem. Soc.*, 2010, **132**, 12537–12539.
29 S. M. Sadat and R. Y. Wang, *RSC Adv.*, 2016, **6**, 44578–44587.
30 K. Ohno, T. Morinaga, S. Takeno, Y. Tsujii and T. Fukuda, *Macromolecules*, 2007, **40**, 9143–9150.
31 J. Midya, M. Rubinstein, S. K. Kumar and A. Nikoubashman, *ACS Nano*, 2020, **14**, 15505–15516.
32 M. Jhalaria, Y. Huang, E. Ruzicka, M. Tyagi, R. Zorn, M. Zamponi, V. García Sakai, B. Benicewicz and S. Kumar, *Macromolecules*, 2021, **54**, 6968–6974.
33 E. Alonso-Redondo, M. Schmitt, Z. Urbach, C. M. Hui, R. Sainidou, P. Rembert, K. Matyjaszewski, M. R. Bockstaller and G. Fytas, *Nat. Commun.*, 2015, **6**, 8309.
34 Q. Li, T. Tarnsangpradit, K. Biniek-Antosiak, Y. Cang, J. Yan, J. Zhang, K. Matyjaszewski, B. Graczykowski, M. R. Bockstaller and G. Fytas, *Macromolecules*, 2026, **59**, 653–662.
35 J. Pyun, S. Jia, T. Kowalewski, G. D. Patterson and K. Matyjaszewski, *Macromolecules*, 2003, **36**, 5094–5104.
36 J. Yan, M. R. Bockstaller and K. Matyjaszewski, *Prog. Polym. Sci.*, 2020, **100**, 101180.
37 J. Lee, Z. Wang, J. Zhang, J. Yan, T. Deng, Y. Zhao, K. Matyjaszewski and M. R. Bockstaller, *Macromolecules*, 2020, **53**, 1502–1513.
38 C. M. Hui, J. Pietrasik, M. Schmitt, C. Mahoney, J. Choi, M. R. Bockstaller and K. Matyjaszewski, *Chem. Mater.*, 2014, **26**, 745–762.
39 N. Gomopoulos, D. Maschke, C. Y. Koh, E. L. Thomas, W. Tremel, H. J. Butt and G. Fytas, *Nano Lett.*, 2010, **10**, 980–984.
40 J. Midya, Y. Cang, S. A. Egorov, K. Matyjaszewski, M. R. Bockstaller, A. Nikoubashman and G. Fytas, *Nano Lett.*, 2019, **19**, 2715–2722.
41 I. E. Psarobas, N. Stefanou and A. Modinos, *Phys. Rev. B: Condens. Matter Mater. Phys.*, 2000, **62**, 278–291.
42 R. Sainidou, N. Stefanou, I. E. Psarobas and A. Modinos, *Comput. Phys. Commun.*, 2005, **166**, 197–240.
43 R. Sainidou, N. Stefanou and A. Modinos, *Phys. Rev. B: Condens. Matter Mater. Phys.*, 2004, **69**, 064301.
44 D. O. Riese and G. H. Wegdam, *Phys. Rev. Lett.*, 1999, **82**, 1676–1679.
45 T. Still, G. Gantzounis, D. Kiefer, G. Hellmann, R. Sainidou, G. Fytas and N. Stefanou, *Phys. Rev. Lett.*, 2011, **106**, 175505.
46 W. Cheng, R. Sainidou, P. Burgardt, N. Stefanou, A. Kiyanova, M. Efremov, G. Fytas and P. F. Nealey, *Macromolecules*, 2007, **40**, 7283–7290.
47 H. Kim, Y. Cang, E. Kang, B. Graczykowski, M. Secchi, M. Montagna, R. D. Priestley, E. M. Furst and G. Fytas, *Nat. Commun.*, 2018, **9**, 2918.

48 A. Chremos and J. F. Douglas, *Phys. Rev. Lett.*, 2018, **121**, 258002.
49 Y. Zhao, R. Yin, H. Wu, Z. Wang, Y. Zhai, K. Kim, C. Do, K. Matyjaszewski and M. R. Bockstaller, *ACS Macro Lett.*, 2023, **12**, 475–480.
50 Y. Cang, A. N. Reuss, J. Lee, J. Yan, J. Zhang, E. Alonso-Redondo, R. Sainidou, P. Rembert, K. Matyjaszewski, M. R. Bockstaller and G. Fytas, *Macromolecules*, 2017, **50**, 8658–8669.
51 D. Schneider, M. Schmitt, C. M. Hui, R. Sainidou, P. Rembert, K. Matyjaszewski, M. R. Bockstaller and G. Fytas, *ACS Macro Lett.*, 2014, **3**, 1059–1063.
52 L. J. Fetters, D. J. Lohse, S. T. Milner and W. W. Graessley, *Macromolecules*, 1999, **32**, 6847–6851.
53 J. D. Ferry, *Viscoelastic Properties of Polymers*, Wiley, New York, 3rd edn, 1980.
54 B. Zuo, C. Li, Q. Xu, K. Randazzo, N. Jiang, X. Wang and R. D. Priestley, *ACS Nano*, 2021, **15**, 9568–9576.
55 A. M. Urbas, E. L. Thomas, H. Kriegs, G. Fytas, R. S. Penciu and L. N. Economou, *Phys. Rev. Lett.*, 2003, **90**, 108302.
56 E. L. Thomas, D. J. Kinning, D. B. Alward and C. S. Henkee, *Macromolecules*, 1987, **20**, 2934–2939.
57 G. C. Gaunaurd and W. Wertman, *J. Acoust. Soc. Am.*, 1989, **85**, 541–554.